Inorganic Chemistry

Article

pubs.acs.org/IC

# Structural Study of the Apatite $Nd_8Sr_2Si_6O_{26}$ by Laue Neutron Diffraction and Single-Crystal Raman Spectroscopy

Tao An,*[†,‡] Alodia Orera,[§] Tom Baikie,[⊥] Jason S. Herrin,[†] Ross O. Piltz,[∥] Peter R. Slater,[¶] Tim J. White,[†] and María L. Sanjuán*[§]

[†]School of Materials Science and Engineering, Nanyang Technological University, 50 Nanyang Avenue, Singapore 639798, Singapore

[§]ICMA, CSIC, Universidad de Zaragoza, 50009 Zaragoza, Spain

[⊥]Energy Research Institute@NTU (ERI@N), Research Technoplaza, Nanyang Technological University, Nanyang Drive, Singapore 637553, Singapore

[∥]Bragg Institute, Australian Nuclear Science and Technology Organisation, Lucas Heights, New South Wales 2234, Australia

[¶]School of Chemistry, University of Birmingham, Edgbaston, Birmingham B15 2TT, U.K.

*Supporting Information*

**ABSTRACT:** A single-crystal structure determination of $Nd_8Sr_2Si_6O_{26}$ apatite, a prototype intermediate-temperature electrolyte for solid oxide fuel cells grown by the floating-zone method, was completed using the combination of Laue neutron diffraction and Raman spectroscopy. While neutron diffraction was in good agreement with $P6_3/m$ symmetry, the possibility of $P6_3$ could not be convincingly excluded. This ambiguity was removed by the collection of orientation-dependent Raman spectra that could only be consistent with $P6_3/m$. The composition of $Nd_8Sr_2Si_6O_{26}$ was independently verified by powder X-ray diffraction in combination with electron probe microanalysis, with the latter confirming a homogeneous distribution of Sr and the absence of chemical zonation commonly observed in apatites. This comprehensive crystallochemical description of $Nd_8Sr_2Si_6O_{26}$ provides a baseline to quantify the efficacy of cation vacancies, oxygen superstoichiometry, and symmetry modification for promoting oxygen-ion mobility.

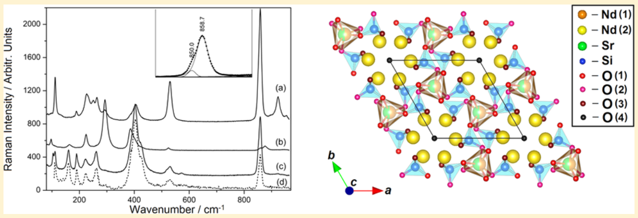

## INTRODUCTION

Lanthanide silicates/germanates $[Ln_{9.33}\square_{0.66}]_{\Sigma 1}[(MO_4)_6][O_2\square_1]$ (Ln = lanthanide; M = Si,Ge; $\square$ = Ln/O vacancy) with apatite structure are promising intermediate-temperature electrolytes for solid oxide fuel cells and show greater oxygen mobility compared to yttria-stabilized zirconia (YSZ) from 500 to 700 °C.[1,2] The structural formula of the prototypical hexagonal apatite ($P6_3/m$) can be expressed as $[A^F_4][A^T_6][(BO_4)_6]X_2$, where A are larger rare-earth or alkaline-earth metals, B are crystallogens or pnictogens, and X are anions. A framework constructed from $A^FO_6$ metaprisms corner-connected to rigid $SiO_4$ tetrahedra encloses one-dimensional *c*-axis tunnels containing the X anions surrounded by $A^T$ cations. The superior oxygen transport of apatites at lower temperatures arises because of the smaller activation energies for interstitial O atoms, compared to vacancy-mediated transport in YSZ,[3,4] which arises when interstitial O atoms are concomitantly introduced with partial filling of Ln vacancies ($2\square_{Ln}^{3+} + 3\square_O^{2-} \rightarrow 2Ln^{3+} + 3O^{2-}$). For example, in $[La_{9.33+2/3x}][(SiO_4)_6][O_{2+3/2x}]$, $0 \le x < 1$,[5] the increasing La content leads to progressively more mobile oxygen,[6] although the putative end member $La_{10}(SiO_4)_6O_3$ ($x = 1$) may not exist. In contrast, the apatite $[La_8Sr_2][(SiO_4)_6[O_2]$ is charge-balanced through $2La^{3+} \leftrightarrow 3Sr^{2+}$ exchange with the absence of superstoichiometric oxygen (26 O atoms per formula unit) and, consequently, shows much lower $O^{2-}$ conductivity than La-rich compositions. To date, the influence of structural defects on oxygen transport in silicate apatites has not been examined rigorously because of the lack of high-quality single crystals. In particular, anisotropic characteristics are rarely reported because this information is not readily extracted from polycrystalline ceramics where pores and grain boundaries attenuate ion transport.[7]

Raman spectroscopy has proven invaluable for identifying interstitial oxide ions,[8,9] order−disorder effects,[10,11] and oxygen dynamics in apatites.[12] However, spectral interpretation has been controversial because of (1) the low occupancy and positional disorder of the mobile oxygen coupled to the infilling of Ln vacancies and/or inclusion of large cation dopants, (2) lower or mixed crystallographic symmetries, and (3) Raman mode overlap in polycrystalline materials. Furthermore, the uniaxial optical character of hexagonal apatites will alter selection rules and introduce spectral artifacts not generally considered.

In this work, we have undertaken a joint neutron diffraction and Raman spectroscopic study of single-crystal $Nd_8Sr_2Si_6O_{26}$.[13] The rare earth chosen was Nd, rather than the more common La, because the former better absorbs IR wavelengths and provides a more stable melt during crystal growth.[7] Despite their low

**Received:** July 1, 2014
**Published:** August 20, 2014

© 2014 American Chemical Society

conductivity, stoichiometric $Ln_8A_2Si_6O_{26}$ apatites are of interest because the elimination of cation vacancies, and very low interstitial O content, provides a baseline chemical and crystallographic model onto which the contributions of different defect types toward oxygen mobilization are overlaid. Single-crystal Raman spectroscopy most clearly identifies mode symmetries and reveals the angular dependence of mode intensities affected by uniaxial character. The results presented here for $Nd_8Sr_2Si_6O_{26}$ provide reference crystallochemistry to further the investigation of nonstoichiometry apatite electrolytes.

## ■ EXPERIMENTAL METHODS

The $Nd_8Sr_2Si_6O_{26}$ single crystal (Figure 1) was grown using the floating-zone technique.[14] An earlier reconnaissance study found that anisotropic ionic conductivity was consistent with crystal chemical characterization by scanning transmission electron microscopy and a preliminary single-crystal X-ray diffraction analysis.[13] In this work, a portion of the single crystals was sectioned and pulverized for analysis by powder X-ray diffraction (PXRD) for comparison with single-crystal neutron diffraction. Patterns were accumulated on a Bruker D8 Advance diffractometer using Cu K$\alpha$ X-rays generated at 40 kV and 40 mA, from $2\theta = 10$ to 130° with a step size of 0.02° and a dwell time of 1.2 s step$^{-1}$. The intensity of the strongest reflection was over 10000 counts, and Rietveld refinements were carried out with *TOPAS* software.[15] Quantitative wavelength-dispersive X-ray spectroscopy was performed on a mirror-polished specimen with field emission source electron probe X-ray microanalysis (EPMA; JXA-8530F). A 15 nm conductive carbon coating was applied to the sample prior to analysis. Point analyses were acquired using a 10-$\mu$m-diameter beam with a current of 40 nA and an accelerating voltage of 15 kV. X-ray lines were monitored using the spectrometer crystals indicated: Si K$\alpha$ (TAP), Sr L$\alpha$ (PET), Nd L$\alpha$ (LIF-H), and O K$\alpha$ (LDE1-H), with peak counting times of 20 s for O, Si, and Nd and 40 s for Sr. Background measurements bracketed each peak for combined counting times equaling the corresponding peak counting times, with the exception of Si, for which a slope factor was applied to a single background measurement in order to avoid interference from Sr L-lines. The measured peak and background regions of all analytes were free of interferences within the sample and standard matrixes. Results were quantified against well-characterized natural and synthetic external calibration standards. The reproducibility of repeat analysis of standards was within 1% of the measured values using the Armstrong/Love Scott[16] matrix correction algorithm and the FFAST mass absorption coefficient data set.[17,18]

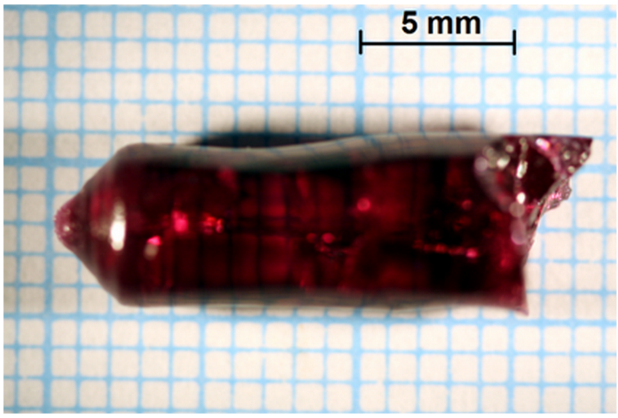

**Figure 1.** $Nd_8Sr_2Si_6O_{26}$ single crystal grown via the floating-zone method.

Single-crystal neutron diffraction patterns were collected at 100 K on the Koala Laue diffractometer at the Open Pool Australian Lightwater reactor operated by the Australian Nuclear Science and Technology Organisation. This Laue diffractometer uses polychromatic thermal neutrons coupled with a large solid-angle (8 steradians) cylindrical image-plate detector. An $Nd_8Sr_2Si_6O_{26}$ crystal of approximate dimensions 1.5 × 1.5 × 1.5 mm was mounted on an aluminum pin with silicone grease. The diffraction patterns were indexed using *LAUEGEN*[19,20] and the reflections integrated using a 2D version of the $\sigma(I)/I$ algorithm described by Wilkinson et al.[21] and Prince et al.[22] No absorption correction was necessary. The reflections were normalized to the same incident wavelength using a curve derived by comparing equivalent reflections and multiple observations via the program *LAUENORM*.[23] Only reflections with wavelengths between 1.0 and 2.9 Å were accepted for the normalization procedure because those outside this range were too weak or had too few equivalents to allow determination of the normalization curve confidently. The structure was determined using *Jana 2006*[24] with the starting model derived from single-crystal X-ray diffraction.[25] *VESTA*[26] was used for 3D visualization of the difference Fourier maps to identify structural disorder.

Raman measurements were recorded in backscattering geometry on selected planes of the single crystals using a DILOR XY spectrometer with excitation through an X10 microscope objective lens. Entrance and exit polarizers were used to minimize polarization losses. Initially, different excitation wavelengths allowed discrimination of Raman bands and possible $Nd^{3+}$ emission lines with $\lambda_{laser} = 496.5$ nm found optimal in order to avoid $Nd^{3+}$ luminescence bands overlapped with the Raman bands.

## ■ RESULTS AND DISCUSSION

**Composition Analysis by EPMA.** Chemical compositions were determined by EPMA analyses (10 replicates), and the atomic abundance normalized to six Si atoms as B-site nonstoichiometry is unlikely (Table S1 in the Supporting Information, SI). The mean element totals are within 1% of unity, suggesting >99% accuracy. The O concentration was derived from measured values of O K$\alpha$. The reproducibility of concentration values for replicates was <1% relative standard deviation for all elements, with the exception of Sr (1.3%), indicating that the sample is homogeneous at the precision of this methodology. The resultant cation abundances are within error of the idealized formula $Nd_8Sr_2Si_6O_{26}$. O yields a slightly higher value of $26.37 \pm 0.23$ atoms that may reflect genuine excess, but caution must be exercised because of the uncertainty in the thickness of the conductive carbon coating applied to the sample surface, compared to the standards and the relatively high absorption of O K$\alpha$ by C.[27]

**Structure Solution by Laue Neutron Diffraction.** Masubuchi et al. reported $P6_3/m$ symmetry for $Nd_8Sr_2Si_6O_{26}$.[28] In this model, Sr solely locates at the $Nd^F(1)$ site, and $[Sr/Nd(1)]O_6$ metaprisms are corner-connected to the $SiO_4$ tetrahedra [each consists of one O(1), one O(2), and two O(3)] to form a framework structure[29] that surrounds $Nd^T(2)$ and O(4) in the tunnel (Figure 2). However, a separate study on the La analogue ($La_8Sr_2Si_6O_{26}$) found $P6_3$ symmetry,[30] in which the 4f cation site splits into two 2b sites and the 12i O(3) site splits into two 6c sites, O(3) and O(4), with O(5) being the tunnel $O^{2-}$ site. Given this ambiguity, neutron diffraction data were tested against both $P6_3/m$ and $P6_3$ (Tables 1 and 2). For the higher symmetry, the determination found that Sr locates solely at the $Nd^F$ 4f site. In lower symmetry $P6_3$, this 4f site splits into two 2b sites, but unexpectedly the refinement converged to a favored distribution of Sr to one ($^1/_3$, $^2/_3$, $z$) site, which led to a better goodness-of-fit (GOF) of 1.24, compared to 1.48 with the $P6_3/m$ model. However, it was readily shown to be a statistical artifact because calculations performed with an equal distribution of Nd:Sr constrained across the two 2b sites gave identical GOFs and only slightly increased reliability values (GOF = 1.24; $R = 6.60\%$; $R_w = 3.32\%$). To investigate Sr partitioning further, high-quality PXRD data from pulverized $Nd_8Sr_2Si_6O_{26}$ was undertaken to better separate Nd:Sr. Rietveld refinement of these PXRD data starting with the $P6_3$ model derived from the single-crystal

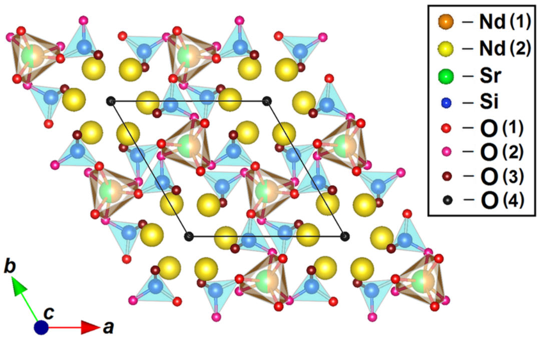

**Figure 2.** Apatite structure of $Nd_8Sr_2Si_6O_{26}$ with $P6_3/m$ symmetry. The Nd(1) and Sr dopant atoms occupy the framework sites (4f), and their occupancy is represented by the filled area of the sphere. Each Nd(1)/Sr forms a metaprism with three O(1) atoms (6h) and three O(2) atoms (6h). A framework structure is formed when these metaprisms are corner-connected to $SiO_4$ tetrahedra [with centered Si (6h) bonded to one O(1) (6h), one O(2) (6h), and two O(3) atoms (12i)]. This framework surrounds the Nd(2) atoms (6h), which, in turn, enclose the O(4) atoms (2a) located along the *c*-axis tunnel.

**Table 1. Specimen Dimensions of the $Nd_8Sr_2Si_6O_{26}$ Crystal, Parameters of Neutron Diffraction, and Lattice Parameters**

| | | |
|---|---|---|
| cryst size ($mm^3$) | 1.5 × 1.5 × 1.5 | 1.5 × 1.5 × 1.5 |
| cryst syst | hexagonal | hexagonal |
| space group | $P6_3/m$ (No. 176) | $P6_3$ (No. 173) |
| temperature (K) | 100 | 100 |
| unit cell dimens | | |
| *a* (Å) | 9.5812(3) | 9.5812(3) |
| *c* (Å) | 7.0655(5) | 7.0655(5) |
| *V* ($Å^3$) | 561.71(5) | 561.71(5) |
| density (g $cm^{-3}$) | 5.6515 | 5.6702 |
| $\mu$ ($cm^{-1}$) | 0.029 | 0.029 |
| wavelength (Å) | 0.71069 | 0.71069 |
| collection limits ($\theta$, deg) | 3.79−41.31 | 3.79−41.31 |
| data measd | 2006 | 2006 |
| unique reflns | 1016 | 1924 |
| reflections with $I \geq 3\sigma(I)$ | 774 | 1412 |
| *R* | 0.0567 | 0.0658 |
| $R_w$ | 0.0344 | 0.0331 |
| GOF | 1.48 | 1.24 |
| D residual (fm $Å^{-3}$) | | |
| + | 0.90 | 0.69 |
| − | 0.95 | 0.79 |

neutron diffraction refinements with only instrumental parameters and Nd/Sr cation occupancies released showed no preference for the Nd and Sr over the two alternative 2b sites. Thus, there was no case to support Nd/Sr ordering over the framework $Ln^FO_6$ metaprisms (see Figure S1 in the SI for the PXRD refinement profile and the distribution of Nd/Sr over the 2b sites). Also, no supercell reflections were observed in either the neutron or X-ray diffraction studies to indicate such ordering of the Nd/Sr cations, which was justified by a parallel transmission electron microscopy study (to be published elsewhere).[13] Therefore, the correct symmetry could not be discerned between $P6_3/m$ and $P6_3$ solely by X-ray or neutron diffraction, and Raman spectroscopy was thus performed, as described in the subsequent section. Table 3 contains the anisotropic atomic displacement parameters, while Tables S2 and S3 in the SI show selected bond lengths, angles, and bond valence sums from the neutron refinements in each space group.

EPMA measures the local compositions to a depth of ∼1 $\mu$m, was in agreement with neutron diffraction that inspects the entire volume of the crystal shard, and yielded the refined composition $Nd_{8.0(2)}Sr_{2.0(2)}Si_6O_{26}$ ($P6_3/m$). This agrees well with the idealized value and provides further confirmation of the chemical homogeneity at the millimeter scale. Nonetheless, difference Fourier maps reveal weak intensity centers, possibly arising from low-occupancy interstitial O sites. The atomic positions and interatomic distances to the respective nearest atomic neighbors for these Fourier peaks are listed in Table 4. In addition, from the Fourier intensity and neutron scattering lengths (Table S4 in the SI), the O concentration at each interstitial site can be calculated (Figure 3). Some of these potential interstitial O sites are close to the $SiO_4$ tetrahedra and likely to promote localized structural distortion because the $SiO_4$ units (being essentially rigid bodies) tilt away from their ideal locations. Such tilting is characteristic of apatites, as has recently been described for mimetite $[Pb_{10}(AsO_4)_6Cl_2]$,[31] where $AsO_4$ tetrahedra rotate to accommodate the stereochemically active $6s^2$ lone-pair electrons of $Pb^{2+}$, leading to a monoclinic supercell ($a_{mon} = b_{mon} = 2a_{hex}$; $c_{mon} = c_{hex}$). In the present context, it is possible that the $Pb^{2+}$ lone-pair electrons in $Pb_{10}(AsO_4)_6Cl_2$ occupy positions similar to those of the interstitial O atoms of the electrolyte material because stereochemically active lone pairs are of a volume similar to that of an $O^{2-}$ ion.[32,33] However, for $Nd_8Sr_2Si_6O_{26}$, the low abundance of interstitial O atoms does not drive the formation of a supercell, nor can they be detected as neutron scattering centers in the single crystal.

**Raman Spectral Characteristics of $P6_3/m$ and $P6_3$ Symmetry.** For $P6_3/m$ $Nd_8Sr_2Si_6O_{26}$, there are 33 Raman active modes ($12A_g + 8E_{1g} + 13E_{2g}$), where 15 belong to $SiO_4$ internal modes, 4 to $SiO_4$ librations, and 14 to Nd, $SiO_4$, and O(4) translations (Table 5). Internal modes for an isolated and regular tetrahedron are $\nu_1$ (symmetric stretching), $\nu_2$ (symmetric bending), $\nu_3$ (asymmetric stretching), and $\nu_4$ (asymmetric bending), and in silicate apatites, they typically appear at $\nu_1 \sim 850$ $cm^{-1}$, $\nu_3 \sim 930$ $cm^{-1}$, $\nu_2 \sim 400$ $cm^{-1}$, and $\nu_4 \sim 530$ $cm^{-1}$.[8−10,12,34] Insertion of the tetrahedron into a crystal lattice splits the number of modes by lowering of the symmetry and through correlated vibrations between different tetrahedra. These effects lead to the appearance of multiple bands in the regions of $\nu_1$, $\nu_2$, $\nu_3$, and $\nu_4$ (Table 6).

Should the symmetry be lowered to $P6_3$, the number of Raman active modes increases to 63 (Table 7), which decomposes as $21A + 21E_1 + 21E_2$. For completeness, decomposition of the 27 internal modes expected in this space group is given in Table 6. Removing the inversion symmetry activates in Raman spectral polar modes that manifest with different frequencies according to their longitudinal or transverse character. Because A and $E_1$ modes are polar, the observed frequencies should multiply to 105 ($21A_{TO}$, $21A_{LO}$, $21E_{1,TO}$, $21E_{1,LO}$, and $21E_2$, where "LO" and "TO" denote longitudinal and transverse-optical modes, respectively).

The Raman tensors, $R_{is}$, for $6/m$ symmetry (as in $P6_3/m$) are

$$A_g = \begin{pmatrix} a & & \\ & a & \\ & & b \end{pmatrix}$$

$$E_{1g} = \begin{pmatrix} & & c \\ & & d \\ c & d & \end{pmatrix}\begin{pmatrix} & & -d \\ & & c \\ -d & c & \end{pmatrix}$$

Table 2. Refined Atomic Positions, Site Occupancy, and Isotropic Atomic Displacement Parameters from Laue Neutron Diffraction of $Nd_8Sr_2Si_6O_{26}$ at 100 K[a]

| site | Wyckoff | $x$ | $y$ | $z$ | occupancy | $U_{iso}$ |
|---|---|---|---|---|---|---|
| | | | $P6_3/m$ | | | |
| Nd(1) | 4f | $^1/_3$ | $^2/_3$ | −0.00015(9) | 0.49(5) | 0.0074(2) |
| Sr | 4f | $^1/_3$ | $^2/_3$ | −0.00015(9) | 0.51(5) | 0.0074(2) |
| Nd(2) | 6h | 0.01063(5) | 0.24229(5) | $^1/_4$ | 1 | 0.0060(2) |
| Si | 6h | 0.3983(1) | 0.3699(1) | $^1/_4$ | 1 | 0.0065(3) |
| O(1) | 6h | 0.31607(9) | 0.48180(9) | $^1/_4$ | 1 | 0.0127(2) |
| O(2) | 6h | 0.59438(8) | 0.47298(8) | $^1/_4$ | 1 | 0.0117(2) |
| O(3) | 6h | 0.34076(7) | 0.25096(6) | 0.06767(8) | 1 | 0.0140(2) |
| O(4) | 2a | 0 | 0 | $^1/_4$ | 1 | 0.0144(3) |
| | | | $P6_3$ | | | |
| Nd(1) | 2b | $^1/_3$ | $^2/_3$ | −0.0027(3) | 0.04(7) | 0.0063(5) |
| Sr | 2b | $^1/_3$ | $^2/_3$ | −0.0027(3) | 0.96(7) | 0.0063(5) |
| Nd(2) | 2b | $^2/_3$ | $^1/_3$ | −0.0024(3) | 1 | 0.0087(5) |
| Nd(3) | 6c | 0.01067(4) | 0.24234(4) | 0.2490(3) | 1 | 0.0061(1) |
| Si | 6c | 0.39836(8) | 0.36986(9) | 0.2457(5) | 1 | 0.0065(2) |
| O(1) | 6c | 0.31609(7) | 0.48174(7) | 0.2486(4) | 1 | 0.0128(2) |
| O(2) | 6c | 0.59433(6) | 0.47299(7) | 0.2485(5) | 1 | 0.0118(2) |
| O(3) | 6c | 0.3423(2) | 0.2514(2) | 0.0660(3) | 1 | 0.0131(6) |
| O(4) | 6c | −0.3390(3) | −0.2506(2) | −0.0692(3) | 1 | 0.0155(7) |
| O(5) | 2a | 0 | 0 | 0.2538(8) | 1 | 0.0140(3) |

[a] The Sr was found to solely locate at the 4f site in the $P6_3/m$ model and the ($^1/_3$, $^2/_3$, $z$) 2b site in the $P6_3$ model.

Table 3. Refined Anisotropic Atomic Displacement Parameters from Laue Neutron Diffraction of $Nd_8Sr_2Si_6O_{26}$ at 100 K

| site | $U_{11}$ | $U_{22}$ | $U_{33}$ | $U_{12}$ | $U_{13}$ | $U_{23}$ |
|---|---|---|---|---|---|---|
| $P6_3/m$ | | | | | | |
| Nd(1)/Sr | 0.0091(2) | 0.0091(2) | 0.0040(3) | 0.0046(1) | 0 | 0 |
| Nd(2) | 0.0063(2) | 0.0064 (2) | 0.0051(2) | 0.0029(2) | 0 | 0 |
| Si | 0.0072(3) | 0.0064(3) | 0.0063(4) | 0.0036(3) | 0 | 0 |
| O(1) | 0.0166(3) | 0.0127(3) | 0.0134(3) | 0.0109(2) | 0 | 0 |
| O(2) | 0.0082(3) | 0.0096(3) | 0.0152(4) | 0.0028(2) | 0 | 0 |
| O(3) | 0.0231(3) | 0.0115(2) | 0.0084(3) | 0.0094(2) | −0.0061(2) | −0.0028 (2) |
| O(4) | 0.0103(3) | 0.0103(3) | 0.0227(8) | 0.0051(2) | 0 | 0 |
| $P6_3$ | | | | | | |
| Nd(1)/Sr | 0.0084(6) | 0.0084(6) | 0.002(1) | 0.0042(3) | 0 | 0 |
| Nd(2) | 0.0101(5) | 0.0101(5) | 0.006(1) | 0.0051(3) | 0 | 0 |
| Nd(3) | 0.0064(1) | 0.0066(2) | 0.0050(2) | 0.0030(1) | −0.0009(5) | −0.0007(5) |
| Si | 0.0072(3) | 0.0065(2) | 0.0061(3) | 0.0037(2) | −0.0023(9) | −0.0004(9) |
| O(1) | 0.0168(3) | 0.0129(2) | 0.0135(3) | 0.0110(2) | 0.0049(9) | 0.0012(9) |
| O(2) | 0.0082(2) | 0.0097(2) | 0.0153(3) | 0.0028(2) | 0.0002(10) | 0.0020(9) |
| O(3) | 0.0225(8) | 0.0125(7) | 0.010(1) | 0.0131(7) | −0.0097(6) | −0.0083(5) |
| O(4) | 0.0242(9) | 0.0110(7) | 0.007(1) | 0.0055(7) | −0.0027(6) | 0.0028(5) |
| O(5) | 0.0104(3) | 0.0104(3) | 0.0213(8) | 0.0052(1) | 0 | 0 |

Table 4. Interstitial O Positions and Their Respective Peak Concentrations and Nearest Neighbors at 100 K, Arranged from Highest to Lowest Concentration

| | $x$ | $y$ | $z$ | concn (Å$^{-3}$) | nearest to | $x$ | $y$ | $z$ | distance (Å) |
|---|---|---|---|---|---|---|---|---|---|
| $O(1)_{int}$ | 0.7375 | 0.2011 | $^1/_4$ | 0.041 | Si | 0.6302 | 0.0285 | $^1/_4$ | 1.45 |
| $O(2)_{int}$ | 0.3684 | 0.1010 | $^1/_4$ | 0.040 | Nd(2) | 0.2317 | −0.0106 | $^1/_4$ | 1.21 |
| $O(3)_{int}$ | 0.1533 | 0.4994 | 0.1574 | 0.040 | O(1) | 0.3161 | 0.4818 | $^1/_4$ | 1.78 |

$$E_{2g} = \begin{pmatrix} e & f & \\ f & -e & \\ & & \end{pmatrix}\begin{pmatrix} f & -e & \\ -e & -f & \\ & & \end{pmatrix}$$

Raman tensors for the six factor groups (as in the $P6_3$ space group) are the same as those for $6/m$ except for the parity labeling and polarity of the A and $E_1$ modes. The expressions "parallel" and "crossed" will be used for configurations with $e_i \| e_s$ and $e_i \perp e_s$, respectively, where $e_i$ and $e_s$ stand for the polarization directions of the incident and scattered electric fields, respectively.

Mode identification is straightforward if measurements are performed along crystal directions in which only one type of symmetry is active. In addition, the discussion about optical anisotropy is easier if measurements are performed with the $z$ axis

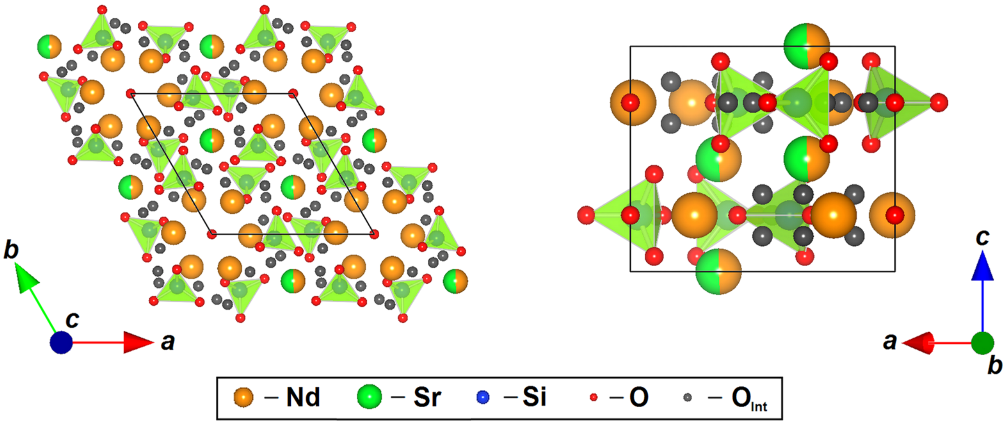

**Figure 3.** Locations of interstitial O atoms in $Nd_8Sr_2Si_6O_{26}$ ($P6_3/m$) at 100 K. No interstitials were found to be in the [001] tunnel.

**Table 5. Raman Activity in $P6_3/m$**

| atom | site | Raman activity in $P6_3/m$[a] |
|---|---|---|
| Nd(1) | 4f | $A_g + E_{1g} + E_{2g}$ |
| Nd(2) | 6h | $2A_g + E_{1g} + 2E_{2g}$ |
| Si | 6h | $2A_g + E_{1g} + 2E_{2g}$ |
| O(1) | 6h | $2A_g + E_{1g} + 2E_{2g}$ |
| O(2) | 6h | $2A_g + E_{1g} + 2E_{2g}$ |
| O(3) | 12i | $3A_g + 3E_{1g} + 3E_{2g}$ |
| O(4) | 2a | $E_{2g}$ |

[a] Total = $12A_g + 8E_{1g} + 13E_{2g}$ (33 modes).

**Table 6. Internal Modes of $SiO_4$ Tetrahedra in $P6_3/m$ and $P6_3$ Space Groups**

| tetrahedra | Raman activity in $P6_3/m$ | no. of modes | Raman activity in $P6_3$ | no. of modes |
|---|---|---|---|---|
| $\nu_2$(E) | $A_g + E_{1g} + E_{2g}$ | 3 | $2A + 2E_1 + 2E_2$ | 6 |
| $\nu_4(T_2)$ | $2A_g + E_{1g} + 2E_{2g}$ | 5 | $3A + 3E_1 + 3E_2$ | 9 |
| $\nu_1(A_1)$ | $A_g + E_{2g}$ | 2 | $A + E_1 + E_2$ | 3 |
| $\nu_3(T_2)$ | $2A_g + E_{1g} + 2E_{2g}$ | 5 | $3A + 3E_1 + 3E_2$ | 9 |
| total | $6A_g + 3E_{1g} + 6E_{2g}$ | 15 | $9A + 9E_1 + 9E_2$ | 27 |

**Table 7. Raman Activity in $P6_3$**

| atom | site | Raman activity in $P6_3$ |
|---|---|---|
| Nd(1) | 2b | $A + E_1 + E_2$ |
| Nd(2) | 2b | $A + E_1 + E_2$ |
| Nd(3) | 6c | $3A + 3E_1 + 3E_2$ |
| Si | 6c | $3A + 3E_1 + 3E_2$ |
| O(1) | 6c | $3A + 3E_1 + 3E_2$ |
| O(2) | 6c | $3A + 3E_1 + 3E_2$ |
| O(3) | 6c | $3A + 3E_1 + 3E_2$ |
| O(4) | 6c | $3A + 3E_1 + 3E_2$ |
| O(5) | 2a | $A + E_1 + E_2$ |

Total = $21A + 21E_1 + 21E_2$ (63 modes).

either perpendicular to the surface or contained in it. Thus, most of the results presented in this work were recorded within a plane that contains the *z* axis so that both the incident and scattered beams are perpendicular to the optical axis (see the scheme in Figure 4). We denote as *u* the direction perpendicular to the *c* axis in such a plane. This *u*−*z* plane provides the crystal directions required for mode identification in the centrosymmetric $P6_3/m$ space group: *zz* and *uz* spectra give $A_g$ and $E_{1g}$ modes, respectively, whereas the *uu* spectrum presents a superposition of $A_g$ and $E_{2g}$ symmetries, which allows identification of the $E_{2g}$ modes.

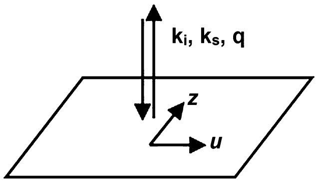

**Figure 4.** Schematic diagram showing the single-crystal surface and the main directions used in this study. $k_i$ and $k_s$ stand for the directions of incident and scattered light; *q* is the direction of phonon propagation. *u* is perpendicular to the *z* axis; both are contained within the horizontal plane.

The situation is more complicated for the noncentrosymmetric space group $P6_3$. As mentioned previously, A and $E_1$ modes are now polar and will manifest with different frequencies depending on their longitudinal or transverse character, which, in turn, depends on the relative orientation of mode propagation (*q*) and polarization (*p*). According to the tables, the polarity of the A modes is along the *z* direction and that of $E_1$ modes is along the $\{x, y\}$ directions. Then, in a backscattering configuration onto the *u*−*z* plane, with $q \perp z$, $A_{TO}$, $E_{1LO}$, and $E_{1TO}$ are the excited components. In contrast, if spectra are collected from the (001) plane ($q \| z$), only the LO component of the A modes would be observed ($E_1$ modes are not active in this plane). In an arbitrary case, with *z* neither parallel nor perpendicular to the direction of incidence, we should expect the simultaneous presence of the LO and TO components of all polar modes. In summary, if the lattice is polar, the A and $E_1$ modes should appear either split or with a different frequency when spectra measured in different planes are compared. The polarity does not affect the behavior of the nonpolar $E_2$ modes.

**Raman Spectral Analysis.** Figure 5 shows *zz*, *uz*, and *uu* spectra of $Nd_8Sr_2Si_6O_{26}$ single crystals recorded at room temperature within the *u*−*z* plane. By comparison to other Si apatites,[12] the bands arising from internal vibrations of $SiO_4$ tetrahedra are readily identified: $\nu_1$ and $\nu_3$ stretching modes around 860 and 920 $cm^{-1}$ and bending modes $\nu_2$ and $\nu_4$ at about 400 and 530 $cm^{-1}$, respectively. These values are slightly higher than those of $La_8Sr_2Si_6O_{26}$ because of the smaller lattice parameters of the Nd compound.[9] Translation external modes are expected below 600 $cm^{-1}$. Vibration of the tunnel oxygen O(4), in particular, is expected at relatively high frequencies on the order of 400−500 $cm^{-1}$,[8] thus possibly overlapping with the bending internal modes. With regards to the libration of $SiO_4$ tetrahedra, they are expected also at low or moderate frequencies (<300 $cm^{-1}$).

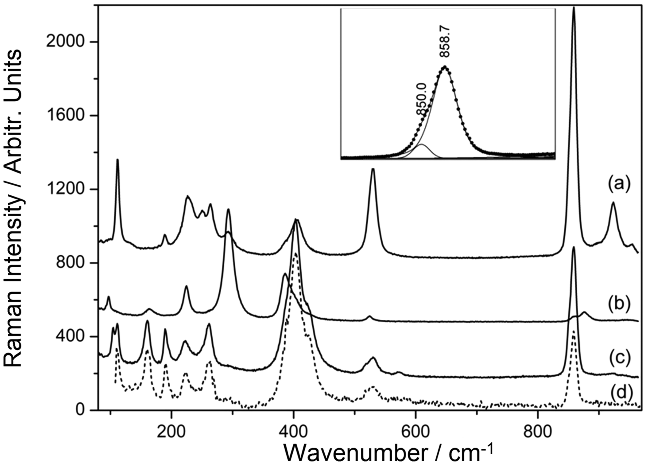

**Figure 5.** Raman spectra of $Nd_8Sr_2Si_6O_{26}$ recorded in (a) *zz*, (b) *uz*, and (c) *uu* configurations within the *u*−*z* plane and (d) the *uu* spectrum measured onto a plane nearly perpendicular to the *z* axis. The inset shows the decomposition of the *zz* spectrum in the region of the $\nu_1$ breathing mode as a sum of pseudo-Voigt profiles. The points are the experimental data, and the lines are a result of the fitting.

**Table 8. Experimental Frequencies and Assignment within the $P6_3/m$ Space GGroup[a]**

| $A_g$ modes ($cm^{-1}$) | $E_{1g}$ modes ($cm^{-1}$) | $E_{2g}$ modes ($cm^{-1}$; from the *uu* spectrum) | assignment |
|---|---|---|---|
| 111.8 | 97.1 | 104.3 | Nd and $SiO_4$ translations and $SiO_4$ librations |
| 127.8 | 132 | | |
| | 164.1 | 160 | |
| 189.2 | 196.7 | 189.6 | |
| 227.8 | 224.3 | 222 | |
| | | 236.3 | |
| 250 | 243.7 | | |
| 264.4 | 259.8 | 261.3 | |
| 292.9 | 293.5 | *290.6 leak* | |
| 386.1 | 384.8 | | $\nu_2$ + O(4) |
| 405 | 395.5 | 403.2 | |
| | *427 leak* | 424.7 | |
| | | 431.6 | |
| | | 517.7 | $\nu_4$ + O(4) |
| 529.6 | 523.8 | | |
| | | *572.9 vw* | |
| 850.2 + 858.7 | *858.7 leak* | 850 +858.6 | $\nu_1$ |
| 895.8 | 876.3 | 888 | $\nu_3$ |
| 923.7 | *924 leak* | 919.8 | |
| 954.1 | 947.7 | 943.5 | |

[a] Numbers in italics indicate weak and broad bands evidenced only through the fitting procedure.

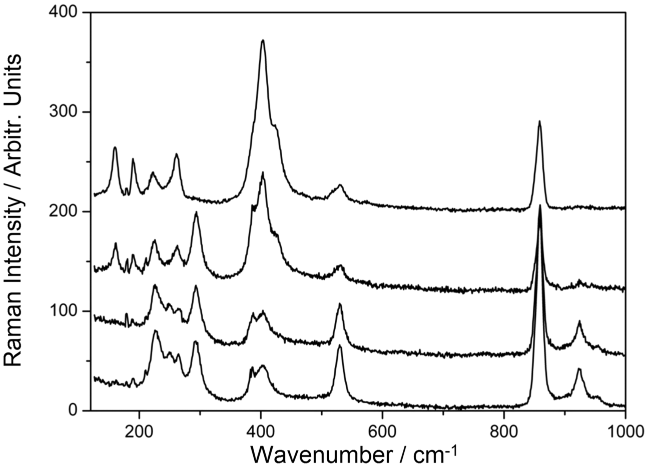

**Figure 6.** Raman spectra of $Nd_8Sr_2Si_6O_{26}$ measured in backscattering geometry onto a *u*−*z* plane of the single crystal, with *u* being an unknown direction within the hexagonal (001) plane, as a function of the angle formed by the incident electric field and the *u* axis. Spectra were recorded in a parallel configuration (the electric field of the scattered light is parallel to that of the incident light). From top to bottom, $\alpha$ = 0°, 35°, 70, and 90°.

The readily identifiable bands are $12A_g$, $8E_{1g}$, and $11E_{2g}$ modes, in close expectation for $P6_3/m$ symmetry ($12A_g + 8E_{1g} + 13E_{2g}$). To have a full picture of the Raman activity and accurate frequencies, spectra were decomposed as a sum of pseudo-Voigt band profiles using *LabSpec* software with position, width, integrated area, and Gaussian/Lorentzian mixing fitted. This procedure accentuates weak and broad bands that might arise from lower symmetry, oxygen disorder coupled to Sr incorporation, or second-order effects (Table 8). Even including the secondary features, the number of observed bands is significantly less than expected for $P6_3$. Moreover, because the LO/TO splitting was not detected for any mode, there is no evidence for long-range symmetry reduction. For example, the *uu* spectra measured in different crystallographic planes appear similar (Figure 5), and the A modes, in particular, present the same frequencies as those in the *zz* spectrum without splitting.

Spectral decomposition also found that the $A_g$ part of the $\nu_1$ band consists of two components (see the inset in Figure 5), with the one at lower frequency (850 $cm^{-1}$) having about one-tenth of the intensity of the main feature at 859 $cm^{-1}$. The splitting of the $\nu_1$ band is quite unexpected in $Nd_8Sr_2Si_6O_{26}$ but has been detected in other apatites, where it has been attributed to perturbation of $SiO_4$ tetrahedra by either nearby cation vacancies or interstitial oxide ions.[10,34] Because previous Raman studies[10] were performed on polycrystalline samples, the superposition of the $E_{2g}$ and $A_g$ components of the $\nu_1$ band may mask the $A_g$ splitting shown in this work. In $Nd_8Sr_2Si_6O_{26}$, without cation vacancies and negligible interstitial O concentration,[35] this splitting may indicate perturbation of the $SiO_4$ tetrahedron caused by disorder on the Nd sublattice induced through the incorporation of Sr.

**Raman Spectra Angular Dependence.** Away from the principal crystal orientations, the selection rules appear to fail in the case of the $A_g$ modes, something that can be explained by the optically anisotropic character of the $Nd_8Sr_2Si_6O_{26}$ apatite. Raman spectra of $Nd_8Sr_2Si_6O_{26}$ were measured in a backscattering configuration within the *u*−*z* plane as a function of the angle ($\alpha$) formed by the electric field and the *u* axis in "parallel" and "crossed" configurations (Figures 6 and 7, respectively). In the absence of uniaxial effects, Raman intensities are proportional to the usual expression

$$I \propto |\sum e_i R_{is} e_s|^2$$

where $R_{is}$, $e_i$, and $e_s$ were defined above. When the appropriate Raman tensors for $A_g$ mode symmetry are made use of, the angular dependences of the mode intensities in the *u*−*z* plane with *u* along an unknown direction (cos $\beta$, sin $\beta$, 0) are expressed as

$$A_g(||) = (a\cos^2\alpha + b\sin^2\alpha)^2 \tag{1}$$

$$A_g(\perp) = (a - b)^2 \sin^2\alpha \cos^2\alpha \tag{2}$$

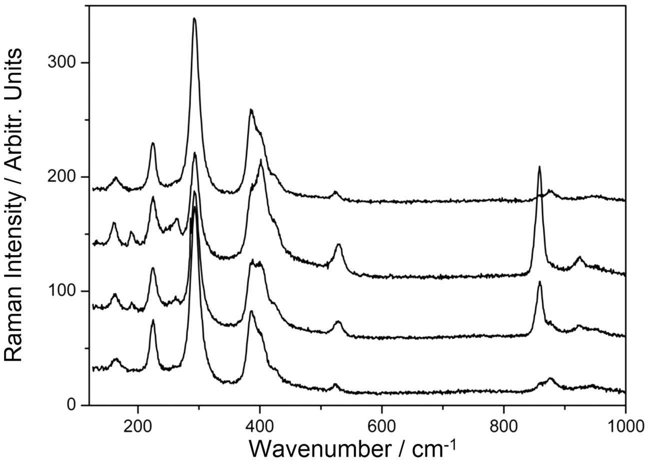

**Figure 7.** Raman spectra of $Nd_8Sr_2Si_6O_{26}$ recorded in a crossed configuration (the electric field of the scattered light is perpendicular to that of the incident light). From top to bottom, $\alpha = 0°, 35°, 70°$, and $90°$.

It is noted that the $\beta$ dependence disappears in the final expressions.

Figure 8 shows the angular dependence of the intensity of the $A_g$ component of the $SiO_4$ breathing mode at 859 $cm^{-1}$ and of the $A_g$ modes at 530 and 925 $cm^{-1}$. When the experimental points (circles) are superimposed on the intensity evolution (dashed line) given by eqs 1 and 2, which simplify to $I = a^2$ and $I = b^2$ for $\alpha = 0$ and $90°$, the correspondence is unsatisfactory. The discrepancy is attributed to the depolarization of light induced by the optical anisotropy of the material. In an optically uniaxial system, the incident light decomposes into two waves: the ordinary wave, propagating with refraction index $n_0$ (ordinary index), and the extraordinary wave, propagating with refraction index $n_{\text{eff}}$, which depends on the angle ($\theta$) formed by the direction of propagation of light and the optical axis in the form

$$\frac{1}{n_{\text{eff}}^2} = \frac{\cos^2\theta}{n_0^2} + \frac{\sin^2\theta}{n_e^2}$$

where $n_e$ is the extraordinary refraction index. The difference between $n_0$ and $n_e$ produces a dephasing between the ordinary and extraordinary waves, which results in depolarization of light as it travels through the medium. For $\theta = 90°$, as in our measurements in the $u-z$ plane, $n_{\text{eff}} = n_e$ and the uniaxial effects are maximized.

These effects are consistent with the formalism of Alonso-Gutiérrez et al.[36] that decomposes the electric field at each step of the Raman process as the sum of ordinary and extraordinary components and introduces a dephasing factor $\exp(i\delta)$ on one of the components, such that

$$\delta = -\frac{2\pi}{\lambda}(n_{\text{eff}} - n_0)d \tag{3}$$

where $\lambda$ is the laser wavelength and $d$ the path run by light either at the entrance or at the exit of the point where the Raman events take place. According to eq 3, $\delta$ is different for each plane ($\theta$) but is the same for all modes and is independent of the measurement angle within the plane, $\alpha$.

It can be shown that the angular dependences for $A_g$ mode intensities for measurement onto a $u-z$ plane are expressed as

$$A_g(\|) = (a\cos^2\alpha\cos 2\delta + b\sin^2\alpha)^2 + a^2\cos^4\alpha\sin^2 2\delta \tag{4}$$

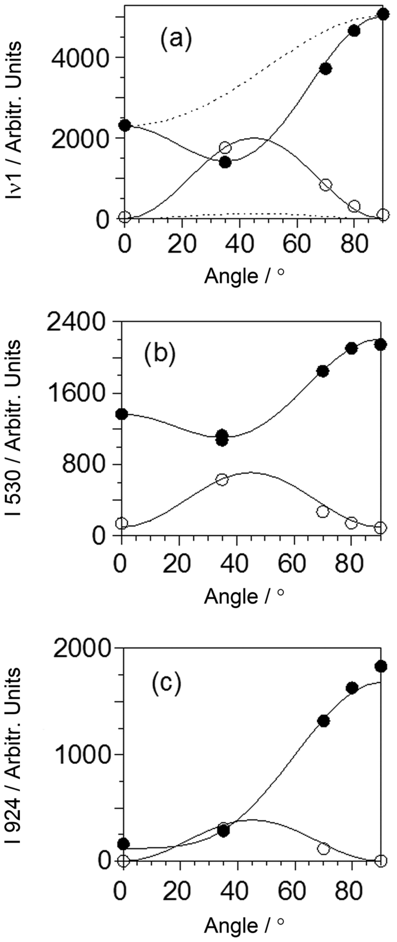

**Figure 8.** Plots of the intensity versus angle dependence for three selected $A_{1g}$ modes. Circles are experimental data for integrated intensities in either parallel or crossed configurations (filled and open symbols, respectively). Solid lines are the best fits using eqs 4 and 5. Dotted lines in part a represent the angular evolution obtained through eqs 1 and 2 without uniaxial effects.

$$A_g(\perp) = (a^2 + b^2 - 2ab\cos 2\delta)\sin^2\alpha\cos^2\alpha \tag{5}$$

These relationships successfully fit the experimental intensities for parallel and crossed configurations within the $u-z$ plane (Figure 8). All three sets of data were fitted with $\delta = 50 \pm 1°$.

As suggested by Alonso-Gutiérrez et al.,[36] a qualitative estimate of the absolute value of the birefringence ($\Delta = n_e - n_0$) can be obtained from the value of $\delta$ and eq 3 provided that the optical path is known. Taking, for instance, $d = 10\ \mu m$, it is found that $|\Delta| = 0.00643$, which is close to the values reported for the apatite phosphate mineral $Ca_{10}(PO_4)_6(OH)_2$.[37]

## ■ CONCLUSIONS

Neutron diffraction of a large untwinned $Nd_8Sr_2Si_6O_{26}$ crystal was indistinguishably modeled in $P6_3/m$ and $P6_3$ models with a slightly improved GOF associated with the latter. In both cases, the refined average compositions conform to the nominal chemistry, as verified by the EPMA study, which found a homogeneous distribution of Sr. The ambiguous structure determination was resolved through Raman spectroscopy, which found modes consistent with the higher symmetry ($P6_3/m$). Moreover, angular-dependent single-crystal Raman spectroscopy detected the optical uniaxial character of hexagonal $Nd_8Sr_2Si_6O_{26}$. The Raman results suggest that any deviation from $P6_3/m$ is so small that it has little effect on the Raman activity. Overall, the results are consistent with centrosymmetric space group $P6_3/m$ because the number of modes is far fewer than expected for $P6_3$ and no LO/TO split frequencies were observed. Splitting of the $A_g$ component of the $SiO_4$ internal mode can be attributed to Sr doping, although a low concentration of Frenkel interstitial oxide ions may also perturb the $SiO_4$ tetrahedra. Optical uniaxial effects are proposed to explain the apparent nonfulfillment of selection rules if spectra are recorded out of the main crystal directions. If there is such a symmetry lowering, analogous to $La_{9.33}Si_6O_{26}$,[30] it gives only broad bands with weak activity.

## ■ ASSOCIATED CONTENT

### Ⓢ Supporting Information

Figure showing the PXRD refinement profile, tables listing EPMA data, selected bond lengths and angles for $P6_3/m$ and $P6_3$, and selected neutron scattering lengths, and CIF files for single-crystal neutron diffraction data in $P6_3/m$ and $P6_3$ symmetry. This material is available free of charge via the Internet at http://pubs.acs.org.

## ■ AUTHOR INFORMATION

### Corresponding Authors

*E-mail: an-tao@imre.a-star.edu.sg.
*E-mail: sanjuan@unizar.es.

### Present Address

‡T.A.: Institute of Materials Research and Engineering (IMRE), 3 Research Link, Singapore 117602, Singapore.

### Notes

The authors declare no competing financial interest.

## ■ ACKNOWLEDGMENTS

This work was supported by A*STAR (Agency for Science, Technology and Research) SERC Grant 082 101 0021 ("Optimization of Apatite Anion Sublattices in Solid Oxide Fuel Cell Electrolytes") and by Spanish Government Grant MAT2010-19837-C06-06. A.O. acknowledges financial support provided by the Spanish Ministerio de Ciencia e Innovación through a Juan de la Cierva contract.

## ■ REFERENCES

(1) Nakayama, S.; Kagayama, T.; Aono, H.; Sadoaka, Y. *J. Mater. Chem.* **1995**, *5*, 1801−1806.
(2) Nakayama, S.; Sakamoto, M. *J. Eur. Ceram. Soc.* **1998**, *18*, 1413−1418.
(3) Kendrick, E.; Islam, M. S.; Slater, P. R. *J. Mater. Chem.* **2007**, *17*, 3104−3111.
(4) Béchade, E.; Masson, O.; Iwata, T.; Julien, I.; Fukuda, K.; Thomas, P.; Champion, E. *Chem. Mater.* **2009**, *21*, 2508−2517.
(5) Tolchard, J. R.; Islam, M. S.; Slater, P. R. *J. Mater. Chem.* **2003**, *13*, 1956−1961.
(6) Jones, A.; Slater, P. R.; Islam, M. S. *Chem. Mater.* **2008**, *20*, 5055−5060.
(7) Higuchi, M.; Masubuchi, Y.; Nakayama, S.; Kikkawa, S.; Kodaira, K. *Solid State Ionics* **2004**, *174*, 73−80.
(8) Smirnov, M.; Sukhomlinov, S.; Mirgorodsky, A.; Masson, O.; Béchade, E.; Colas, M.; Merle-Méjean, T.; Julien, I.; Thomas, P. *J. Raman Spectrosc.* **2010**, *41*, 1700−1707.
(9) Orera, A.; Kendrick, E.; Apperley, D. C.; Orera, V. M.; Slater, P. R. *Dalton Trans.* **2008**, 5296−5301.
(10) Guillot, S.; Beaudet-Savignat, S.; Lambert, S.; Roussel, P.; Tricot, G.; Vannier, R.-N.; Rubbens, A. *J. Raman Spectrosc.* **2011**, *42*, 1455−1461.
(11) Orera, A.; Sanjuan, M. L.; Kendrick, E.; Orera, V. M.; Slater, P. R. *J. Mater. Chem.* **2010**, *20*, 2170−2175.
(12) Lucazeau, G.; Sergent, N.; Pagnier, T.; Shaula, A.; Kharton, V.; Marques, F. M. B. *J. Raman Spectrosc.* **2007**, *38*, 21−33.
(13) An, T.; Baikie, T.; Weyland, M.; Shin, J. F.; Slater, P. R.; Wei, J.; White, A. T. In preparation.
(14) An, T.; Baikie, T.; Wei, F.; Li, H.; Brink, F.; Wei, J.; Ngoh, S. L.; White, T. J.; Kloc, C. *J. Cryst. Growth* **2011**, *333*, 70−73.
(15) *Topas*, version 4.1; Bruker AXS Inc.: Madison, WI, 2008.
(16) Armstrong, J. T. Quantitative analysis of silicates and oxide minerals: Comparison of Monte Carlo, ZAF and $\phi(\rho Z)$ procedures. In *Microbeam Analysis*, Newbury, D. E., Ed.; San Francisco Press, Inc.: San Francisco, CA, 1988; pp 239−246.
(17) Chantler, C. T. *J. Phys. Chem. Ref. Data* **1995**, *24*, 71−643.
(18) Chantler, C. T. *J. Phys. Chem. Ref. Data* **2000**, *29*, 597−1056.
(19) Campbell, J. W. *J. Appl. Crystallogr.* **1995**, *28*, 228−236.
(20) Campbell, J. W.; Hao, Q.; Harding, M. M.; Nguti, N. D.; Wilkinson, C. *J. Appl. Crystallogr.* **1998**, *31*, 496−502.
(21) Wilkinson, C.; Khamis, H. W.; Stansfield, R. F. D.; McIntyre, G. J. *J. Appl. Crystallogr.* **1988**, *21*, 471−478.
(22) Prince, E.; Wilkinson, C.; McIntyre, G. J. *J. Appl. Crystallogr.* **1997**, *30*, 133−137.
(23) Campbell, J. W.; Habash, J.; Helliwell, J. R.; Moffat, K. *Inform. Q. Protein Crystallogr.* **1986**, *18*, 23−31.
(24) Petricek, V.; Dusek, M.; Palatinus, L. *Jana2006. The crystallographic computing system*; Institute of Physics: Praha, Czech Republic, 2006.
(25) An, T.; Baikie, T.; Wei, F.; Pramana, S. S.; Schreyer, M. K.; Piltz, R. O.; Shin, J. F.; Wei, J.; Slater, P. R.; White, T. J. *Chem. Mater.* **2013**, *25*, 1109−1120.
(26) Momma, K.; Izumi, F. *J. Appl. Crystallogr.* **2008**, *41*, 653−658.
(27) Nash, W. P. *Am. Mineral.* **1992**, *77*, 453−457.
(28) Masubuchi, Y.; Higuchi, M.; Takeda, T.; Kikkawa, S. *Solid State Ionics* **2006**, *177*, 263−268.
(29) Baikie, T.; Pramana, S. S.; Ferraris, C.; Huang, Y.; Kendrick, E.; Knight, K. S.; Ahmad, Z.; White, T. J. *Acta Crystallogr., Sect. B* **2010**, *66*, 1−16.
(30) Lambert, S.; Vincent, A.; Bruneton, E.; Beaudet-Savignat, S.; Guillet, F.; Minot, B.; Bouree, F. *J. Solid State Chem.* **2006**, *179*, 2602−2608.
(31) Baikie, T.; Schreyer, M.; Wei, F.; Herrin, J. S.; Ferraris, C.; Brink, F.; Topolska, J.; Piltz, R. O.; Price, J.; White, T. J. *Mineral. Mag.* **2014**, *78*, 325−345.
(32) Andersson, S.; Åstrom, A. *Proc. 5th Mater. Res. Symp.* **1972**, *364*, 3−14.
(33) Moore, P. B.; Shen, J. *Am. Mineral.* **1984**, *69*, 1173−1179.
(34) Wu, R.; Pan, W.; Ren, X.; Wan, C.; Qu, Z.; Du, A. *Acta Mater.* **2012**, *60*, 5536−5544.
(35) An, T.; Baikie, T.; Piltz, R. O.; Meven, M.; Wei, J.; White, T. In preparation.
(36) Alonso-Gutiérrez, P.; Sanjuán, M. L.; Morón, M. C. *Phys. Rev. B* **2005**, *71*, 085205.
(37) Imperial College Rock Library, Online Database. Accessed in 2014.